CHEMISTRY OF MATERIALS

Article

pubs.acs.org/cm

Building Materials from Colloidal Nanocrystal Assemblies: Molecular Control of Solid/Solid Interfaces in Nanostructured Tetragonal ZrO_2

Santosh Shaw,[†] Tiago F. Silva,[‡] Jonathan M. Bobbitt,[§,#] Fabian Naab,[∥] Cleber L. Rodrigues,[‡] Bin Yuan,[⊥] Julia J. Chang,[†] Xinchun Tian,[†] Emily A. Smith,[§,#] and Ludovico Cademartiri*[,†,⊥,#]

[†]Department of Materials Science & Engineering, Iowa State University of Science and Technology, 2220 Hoover Hall, Ames, Iowa 50011, United States

[‡]Instituto de Física da Universidade de São Paulo, Rua do Matão, trav. R 187, 05508-090 São Paulo, Brazil

[§]Department of Chemistry, Iowa State University of Science and Technology, Gilman Hall, Ames, Iowa 50011, United States

[∥]Michigan Ion Beam Laboratory, University of Michigan, Draper Road, Ann Arbor, Michigan 48109, United States

[⊥]Department of Chemical & Biological Engineering, Iowa State University of Science and Technology, Sweeney Hall, Ames, Iowa 50011, United States

[#]Ames Laboratory, U.S. Department of Energy, Ames, Iowa 50011, United States

Supporting Information

ABSTRACT: We here describe a bottom-up approach to control the composition of solid/solid interfaces in nanostructured materials, and we test its effectiveness on tetragonal ZrO_2, an inorganic phase of great technological significance. Colloidal nanocrystals capped with trioctylphosphine oxide (TOPO) or oleic acid (OA) are deposited, and the organic fraction of the ligands is selectively etched with O_2 plasma. The interfaces in the resulting all-inorganic colloidal nanocrystal assemblies are either nearly bare (for OA-capped nanocrystals) or terminated with phosphate groups (for TOPO-capped nanocrystals) resulting from the reaction of phosphine oxide groups with plasma species. The chemical modification of the interfaces has extensive effects on the thermodynamics and kinetics of the material. Different growth kinetics indicate different rate limiting processes of growth (surface diffusion for the phosphate-terminated surfaces and dissolution for the "bare" surfaces). Phosphate termination led to a higher activation energy of growth, and a 3-fold reduction in interfacial energy, and facilitated significantly the conversion of the tetragonal phase into the monoclinic phase. Films devoid of residual ligands persisted in the tetragonal phase at temperatures as high as 900 °C for 24 h.

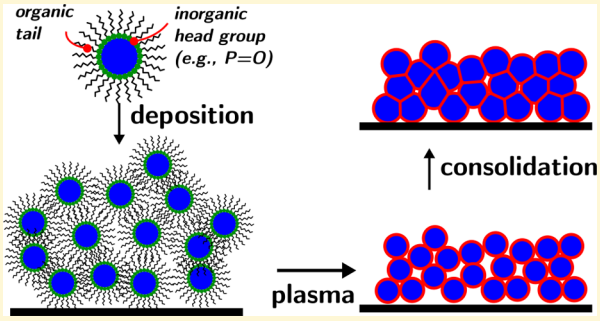

INTRODUCTION

Surfaces and interfaces represent an increasingly important opportunity and challenge. Some of the most exciting recent discoveries in solid state science involve interfaces (or materials that are effectively interfaces): e.g., topological insulators,[1−3] interface superconductivity,[4−7] and graphene.[8,9]

By increasing the fraction of atoms that are at the boundary of a crystal, one can leverage and amplify their unique properties in materials design. As the characteristic length scales of devices approach the atomic scale, the influence of surfaces on their properties becomes increasingly dominant: for most crystals, a radius of curvature of ∼1−2 nm indicates the threshold at which the majority of the atoms are at the surface.[10,11]

Solid/air interfaces have been a subject of intense interest in the past decades. They control the interaction of the material with its environment, with exceptional consequences on its wetting,[12−15] catalytic,[16−20] optical,[21−24] chemical,[25,26] tribological,[27,28] and electrical[1−7,29] properties.

Solid/solid interfaces *within* a material (e.g., the grain boundaries in a polycrystal) are just as important. They can dominate thermal,[30,31] mechanical,[32,33] and bulk transport[34−36] properties, especially in nanostructured materials. They can make thermodynamically unstable phases stable,[37,38] soft metals hard,[39,40] brittle ceramics ductile,[41,42] weak composites tough,[43] and metallic conductors insulating.[29] Nonetheless, compared to solid/air interfaces, they are much more difficult to modify, control, and characterize.

The formation of solid/solid interfaces in a material is usually a direct consequence of the synthesis and processing,[44] after which they are typically inaccessible for modification. Their out-of-equilibrium nature makes them exquisitely sensitive to the exact processing history (e.g., temperature fluctuations leading to diffusion[45]), and composition of the material (e.g.,

Received: July 4, 2017
Revised: August 25, 2017
Published: August 28, 2017

DOI: 10.1021/acs.chemmater.7b02769
Chem. Mater. 2017, 29, 7888−7900

trace elements which segregate to the grain boundaries[46]). Any processing (e.g., high temperatures) that facilitates the evolution of the material toward its thermodynamic ground state tends to compromise the control and design of these interfaces.[47]

To circumvent these difficulties, we have been developing a materials chemistry approach that combines bottom-up solution-based chemistry with top-down physical processing to yield materials with controlled nanostructure (cf. Figure 1).

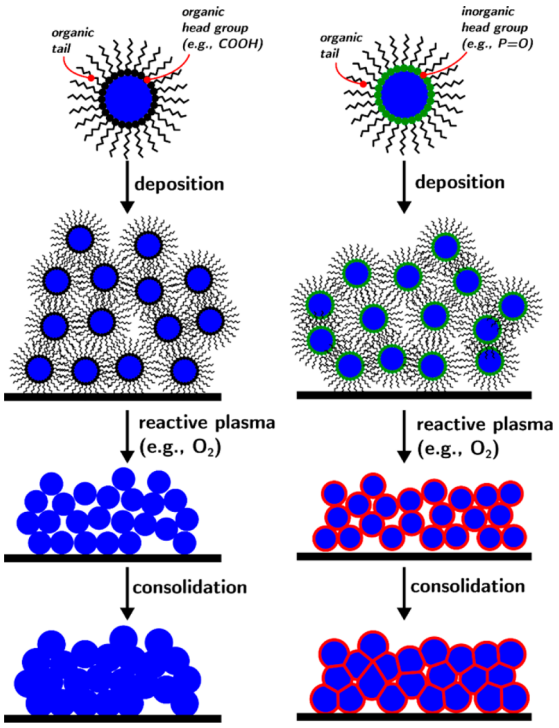

Figure 1. Schematic of bottom-up approach to the control of solid–solid interfaces in nanostructured materials obtained from colloidal nanoparticles. Two scenarios (left and right) are shown. On the left is the case of nanoparticles capped with purely organic ligands. Upon deposition and plasma processing by O_2 plasma, the entirety of the ligand is etched, leaving behind bare surfaces that, upon consolidation, will form bare interfaces. On the right is the case of nanoparticles capped with ligands featuring an inorganic head group. Upon plasma processing with O_2 plasma, the organic tail is removed but the inorganic head group reacts with the plasma, forming nonvolatile groups that are located at the particle surface. Consolidation of the assembly leads to the formation of solids with an engineered solid/solid interface.

Colloidal nanocrystal synthesis can produce a large number of functional nanocrystalline phases (oxides,[48−55] chalcogenides,[56−68] pnictides,[69−78] metals[79−89]) at relatively low temperatures, with remarkable control over crystal size, shape, and surface chemistry. The nanoparticles can be deposited as solids (colloidal nanocrystal assemblies, CNAs[90−92]) constituted of inorganic cores separated by the organic ligands. We have previously shown that the ligands can be completely and selectively removed from thin films of colloidal nanocrystal assemblies by plasma processing.[93−96] While the accompanying volume loss is significant (easily above 40%), we also showed that the structure of the nanoparticle assembly can prevent its cracking, resulting in all-inorganic solid state films:[97] each nanoparticle building block becomes a grain of the resulting nanostructured polycrystal.

We here show that, by combining the control of the ligand shells with the remarkable etch selectivity of O_2 plasma for organics, we can produce all-inorganic solids with monolayer-level control over their solid/solid interfaces. Inorganic elements can react with the O_2 plasma species, but are not etched away since they do not form volatile species, and leave behind a monolayer coating of inorganic phase. Specifically, the O_2 plasma processing of assemblies of nanoparticles of ZrO_2 capped with oleic acid or trioctylphosphine oxide results in ZrO_2 films in which the solid/solid interfaces are, respectively, ZrO_2//ZrO_2 and ZrO_2/phosphate//phosphate/ZrO_2. In contrast to high temperature processing strategies, the plasma we use is dilute and at low pressure and is near room temperature: the processing does not coarsen the particles or damage the interfaces.

This molecularly designed tuning of the interface composition results in significant changes in the macroscopic properties of the material, including grain growth kinetics, phase stability, surface energy, and mechanical properties. Importantly, we show that controlling the solid/solid interfaces allows the stabilization of the tetragonal phase of ZrO_2 to an extent comparable to doping with Y.

There are other approaches that attempt to control interface composition from the bottom-up. Outer shells can be grown on the nanoparticles as a post-synthesis process, leading to core–shell architectures.[61,98−103] These shells are usually thick (several monolayers), they represent a separate phase in the material, and they can dominate the properties of the core,[104] especially when the particle size is <5 nm. The generation of monolayer/submonolayer shells that are uniformly distributed on the surface of the core is not trivial[100] and is a problem that must be solved on a case-by-case basis. Another elegant approach uses inorganic ligands to stabilize nanoparticles:[105] after postprocessing, these ligands can form a matrix.[106]

Homogeneous control of the solid/solid interfaces after consolidation of the materials is a complex problem. Techniques like atomic layer deposition (ALD) can deposit/coat exposed surfaces, thereby filling up the accessible pores. Uniform coating of the surfaces can become more complicated when the pore sizes are <5 nm, which is usually the case for colloidal nanoparticle assemblies. Furthermore, the use of ALD requires one additional step in the processing, while our approach combines the ligand removal with the creation of a designed interface composition.

Most of the above approaches, differently from the one reported here, create a separate phase rather than a pure chemical modification of the interfaces within a single phase material.

RESULTS AND DISCUSSION

Nanoparticle Synthesis and Ligand Exchange. We chose ZrO_2 nanoparticles as our starting inorganic core building block. Zirconia is a highly studied and technologically important ceramic for its mechanical, thermal, and catalytic properties and ionic conductivity. It exists in three crystalline phases: monoclinic, tetragonal, and cubic. The room temperature phase is monoclinic, but tetragonal and cubic phases have superior mechanical, thermal, and catalytic properties and are highly sought for high temperature applications. These phases can be stabilized either by doping[107] or by decreasing crystal size.[38,108]

We synthesized highly crystalline, t-ZrO_2 nanocrystals by an established colloidal synthetic route.[55] Two different ligand

DOI: 10.1021/acs.chemmater.7b02769
Chem. Mater. 2017, 29, 7888−7900

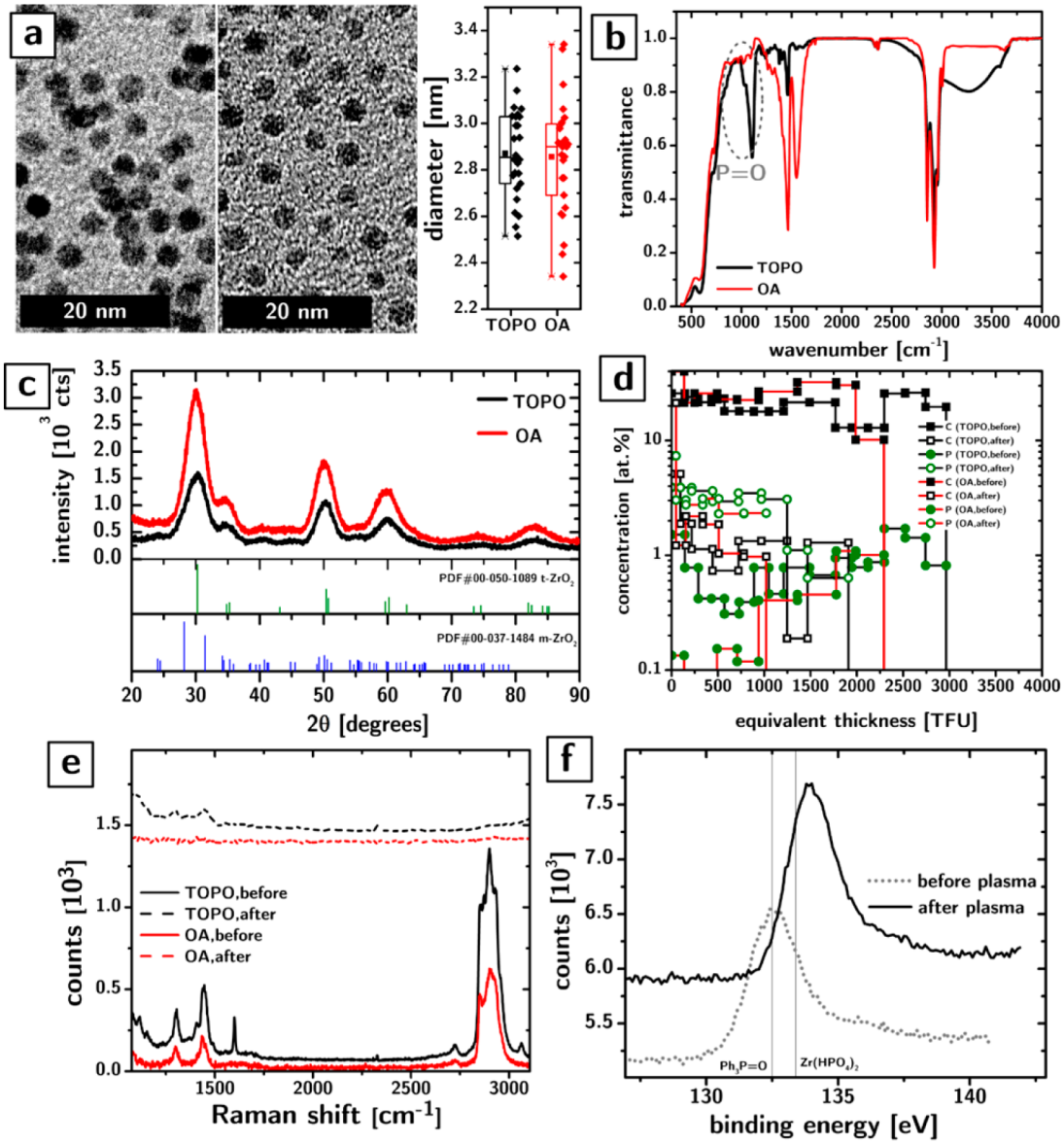

Figure 2. Morphological and chemical characterization of the effect of ligand replacement and plasma processing. (a) TEM micrographs of t-ZrO_2 nanoparticles before and after ligand exchange with OA. On the right is shown the size distribution statistics as a box plot showing no change in the average particle size upon ligand exchange. (b) FT-IR characterization of films obtained from nanoparticles before and after ligand exchange with OA, showing the disappearance of P═O groups. (c) Powder XRD characterization of films obtained from nanoparticles before and after ligand exchange with OA, showing the presence of a single t-ZrO_2 phase. Only trace amounts of monoclinic phase might be observed. (d) Compositional profile of the TOPO and OA samples before and after O_2 plasma processing. The plot shows the homogeneous removal of carbon and preservation of P in the TOPO samples. (e) Raman characterization of TOPO and OA samples before and after O_2 plasma processing confirming the removal of organic fraction of the ligands. (f) XPS characterization of the P $2p_{3/2}$ orbital in TOPO samples before and after plasma processing showing oxidation of phosphine oxide to likely phosphate groups.

shells were produced. The as-synthesized nanocrystals are capped with trioctylphosphine oxide – TOPO ($C_{24}H_{51}PO$). The processing by O_2 plasma etches the octyl chains, and leaves behind the phosphorus, attached to the surface of the nanoparticles. Oleic acid (OA) was chosen as a comparison. It is an established ligand for nanoparticles, and it is fully organic: its etching by O_2 plasma should yield a bare ZrO_2 surface. TOPO was replaced by OA following a simple ligand replacement protocol. For convenience in comparing data, we will refer to the particles before ligand exchange with the shorthand "TOPO", and to the particles after ligand exchange with "OA".

The morphology, size, and crystallinity of the nanoparticles are not affected by the ligand exchange procedure. Figure 2a shows the Transmission Electron Microscopy (TEM) characterization of TOPO and OA samples, as well as their size distribution. While ligand exchange appears to slightly increase the polydispersity (6% vs 8%), the spherical morphology and average size are not significantly affected (2.87 ± 0.07 nm vs 2.86 ± 0.09 nm, where the error is the 95% confidence interval on the average). FT-IR characterization of solid films of TOPO and OA nanoparticles (cf. Figure 2b) shows what appears to be a nearly complete removal of the TOPO ligands after ligand exchange: the absorption peak at 1110 cm^{-1} can be attributed

DOI: 10.1021/acs.chemmater.7b02769
Chem. Mater. 2017, 29, 7888−7900

to the P=O bond in TOPO molecules and nearly vanishes after ligand exchange. Figure 2c shows that the crystallinity of the material is also unaffected: the dominant phase is probably tetragonal[109] before and after ligand exchange, with possible evidence of trace amounts of monoclinic phase (indicated by possible peaks at ~24°, ~41°, and ~45°).

The average distance between TOPO-capped particles calculated from TEM images is ~0.9 nm, whereas the distance between particles after ligand exchange with oleic acid is ~2 nm. Both distances are consistent with TOPO and OA ligand shells that are fully interdigitated. The complete interdigitation of ligands deposited from ZrO_2 nanoparticles dispersions in hexane has been explained elsewhere.[110]

Both TOPO and OA particles were extensively washed with pure solvent (4 times) to avoid unnecessary amounts of free ligands. This is an important factor for the success of the plasma processing since free ligand can reduce the porosity of the colloidal nanoparticle assemblies, and amplify the destructive effects of volume loss on the film integrity.

Particle Deposition and Plasma Processing. Films of TOPO and OA nanoparticles were obtained on Si substrates by spin-coating from hexane dispersions. The concentration of the dispersion and the deposition parameters were controlled to produce 300−400 nm thick films. In both cases, as we described before,[97] this choice of solvent yielded disordered CNAs which resisted cracking upon ligand removal and sintering.

Exposure of ZrO_2 nanocrystals films to plasma serves two purposes: (i) the conversion of CNAs (inorganic cores + organic ligands shells) into all-inorganic solids, and (ii) "programming" the interface composition of the nanocrystals by reaction with the inorganic components of the ligand shell.

Plasma processing was conducted in an inductively coupled plasma chamber at 30 W of power, a pressure of 500 mTorr, and for 48 h, using ultrapure O_2 as feed gas. The effect of this processing on the chemical makeup of the films was determined by Ion Beam Analysis (IBA). Modeling of the IBA characterization allows for the determination of the concentration of individual elements across the sample thickness. Figure 2d shows the concentration of carbon (black scatters) and phosphorus (green scatters) in units of at. %, as a function of the equivalent thickness in thin film units (TFU, 10^{15} atoms/cm^2). The zero value of equivalent thickness in the plot represents the position of the substrate, but, since IBA does not obtain signals from voids in the sample, the equivalent thickness is only a monotonic function of the physical thickness.

In both the TOPO (black line) and OA (red line) samples, the homogeneous ~25 at. % concentration of carbon in the as-deposited films (filled scatters) is reduced to ~1 at. % after plasma processing (empty scatters) throughout the thickness of the CNA. This loss of ligands is accompanied by a shrinkage of the CNA perpendicularly to the substrate by 36% and 45% for TOPO and OA samples, respectively. We have not been able so far to reduce the concentration of carbon much below this value under any processing conditions or times, which leads us to postulate that this residual carbon can be attributed to adventitious contamination[111] that occurs between the plasma processing and the IBA characterization: a 1% volume fraction accounts for much less than a monolayer coverage of the CNA surfaces and some contamination is plausible, especially considering the expectedly high surface energies of these surfaces (γ = 1.02 J/m^2). The decrease in the carbon concentration was supported by Raman scattering (cf. Figure 2e), which shows the disappearance of the main C-H band at 2800−3000 cm^{-1} after plasma processing.

The phosphorus concentration in the TOPO samples remains homogeneous throughout the thickness of the film after plasma processing (cf. Figure 2d), indicating that phosphorus species have not been displaced over hundreds of nanometers. The overall amount of phosphorus is largely unaffected (2.279×10^{16} atoms/cm^2 before plasma vs 2.184×10^{16} atoms/cm^2 after plasma), but its chemical state is significantly modified, as shown by X-ray photoelectron spectroscopy (XPS) in Figure 2f. The P $2p_{3/2}$ peak at 132.5 eV in the TOPO CNAs before plasma processing is comparable to the peak position of Ph_3PO[112] (132.5 ± 0.2 eV from the NIST XPS Database: the value is the average over all entries in the database). Plasma processing causes the peak to shift significantly to higher binding energies (~133.9 eV), consistent with the oxidation expected in an O_2 plasma environment. The peak position is consistent with a complete oxidation of the phosphine oxide group to phosphate (133.4 ± 0.5 eV for zirconium hydrogen phosphate $Zr(HPO_4)_2$ according to the NIST XPS Database: again, the value is averaged over the multiple entries in the database).[112]

Comparisons of the Zr 3d core-line of the TOPO and OA CNAs after plasma processing (see the Supporting Information) are consistent with the above attributions. The binding energies of the TOPO samples are 0.5 eV higher than that in the OA sample (182.9 eV vs 182.4 eV), consistently with the trend observed in the literature (183.9 ± 0.9 eV for $Zr(HPO_4)_2$ vs 183.1 ± 0.7 eV for ZrO_2). The full width at half-maximum (fwhm) of the XPS peaks for oxides like ZrO_2 is influenced by the metal−oxygen bond length or the metal−oxygen coordination number.[113] The fwhm of the Zr $3d_{5/2}$ peak in TOPO samples is ~0.2 eV narrower than that in the OA samples, consistently with the difference reported between $Zr(HPO_4)_2$ and yttria-stabilized zirconia (YSZ).[113]

Combining the complete and extremely accurate elemental analysis provided by IBA characterization, the knowledge of the particle sizes, the identity of the phases, and the film thickness allows, with few assumptions, the determination of the volume fractions of all phases in the CNA. The results of this analysis (detailed in the Supporting Information) for the TOPO and OA samples, before and after plasma processing, are listed in Table 1 and provide important information about the structure of the films and how it is affected by plasma processing. The bottom two rows provide binned volume fractions of the solid

Table 1. Volume Fractions of Different Phases in the Different Types of Colloidal Nanoparticle Assemblies, before and after O_2 Plasma Processing

	TOPO before plasma	TOPO after plasma	OA before plasma	OA after plasma
ZrO_2	0.26	0.43	0.21	0.44
ligands	0.45	0.00	0.52	0.00
phosphate	0.00	0.15	0.00	0.05
chloride	0.02	0.03	0.01	0.03
adventitious C	0.03	0.02	0.00	0.03
H_2O	0.10	0.35	0.09	0.40
pores	0.13	0.00	0.18	0.00
adventitious C + H_2O + air	0.26	0.37	0.27	0.43
filling fraction	0.74	0.63	0.73	0.57

DOI: 10.1021/acs.chemmater.7b02769
Chem. Mater. 2017, 29, 7888−7900

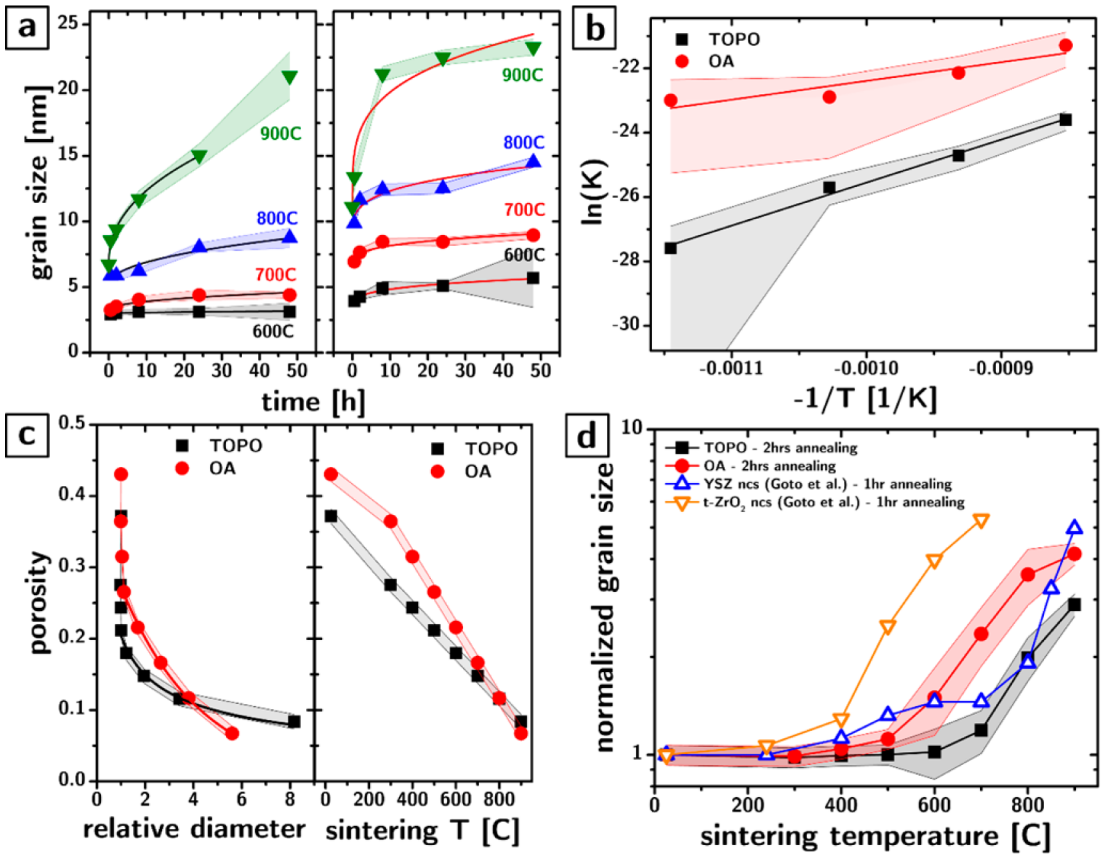

Figure 3. Impact of interface composition on grain growth kinetics. (a) Plots of grain size as a function of time and temperature for TOPO (left) and OA (right) samples. The lines are fits obtained from an Ostwald ripening model. (b) Arrhenius plot for TOPO and OA samples obtained from rate constants obtained from the fits in panel (a). (c) Plot of the relation between porosity on diameter (left) and sintering temperature (right) for both the TOPO and OA samples. The curves show fits of the data to a power law expected for pore coalescence-driven growth. (d) Coarsening at various temperatures. The graph compares our TOPO and OA samples for two or more hours, with YSZ and t-ZrO_2 samples previously reported.[128] In all the above panels, shaded areas behind data points identify the 95% confidence interval on the average value.

(i.e., the filling fraction) and of everything else (i.e., adsorbed water, contaminants, and pore space).

The assumptions used to obtain the numbers in Table 1 are the following: (i) the particles are spherical; (ii) the phases (e.g., ZrO_2) are stoichiometric; (iii) the density of the phases is the same as in their bulk state; (iv) any O atom that could not be attributed to the ZrO_2 or to the ligands/phosphate was attributed to physisorbed H_2O and, to the degree that it was possible, to hydroxils on the surface of the particles; and (v) all Cl (trace amounts originating from the Zr precursor used in the synthesis) was attributed to Cl− groups coordinating surface Zr, and (vi) all P in the plasma-processed samples was assumed to be bound TOPO/phosphate in light of the data in Figure 2f.

The filling fraction of the CNA before plasma processing (0.73−0.74) is very close to the value expected from an fcc packing. Nonetheless, the films produced in these conditions are disordered.[97] The discrepancy can be understood by realizing the 74% filling fraction for fcc packing is true for hard spheres. Before plasma processing, the particles are coated with a ligand shell that is soft and can fill space more effectively. In line with this interpretation, the filling fraction after plasma processing (63% and 57% for TOPO and OA samples, respectively) is consistent with a disordered array and our previous reports.[97] The lower filling fraction in the OA samples is consistent with the longer length of the OA ligands (and the resulting larger separation between the particles in the plane of the film), leading to a more open packing.

The volume fraction of ligands before plasma processing is very large (45% and 52% for TOPO and OA, respectively), but corresponds to a reasonable ligand coverage (20% and 31% of the available binding sites, for TOPO and OA, respectively). After plasma processing, the footprint associated with P triples: the P═O bond turns into a phosphate PO_4^{3-}, yielding a surface coverage of ∼60%. Once two opposing surfaces face each other upon ligand etching, the phosphate layers are expected to form a nearly continuous monolayer.

The volume fraction of H_2O in the ligand-free samples is remarkably large and precisely the amount needed to completely fill the pores. While we do not have analytical information about the size of the pores, simple geometric arguments indicate that they should be, on average, on the order of 2 nm or less. In normal humidity conditions, capillary condensation of water would occur in such micropores. While the amount of water might seem implausible at first glance, it corresponds to a 0.36−0.39 nm layer of water on each nanoparticle, which is approximately 1 monolayer (∼0.31 nm for a H_2O molecule lying flat). Characterization of the plasma processed films by FT-IR supports these findings regarding water and suggests that the observed residual carbon is indeed adventitious carbon in the form of carbonate groups (specifically, bidentate bicarbonate b-HCO_3^- and polydentate

DOI: 10.1021/acs.chemmater.7b02769
Chem. Mater. 2017, 29, 7888−7900

carbonate p-CO_3^{2-}) that could result from the reaction of CO_2 with exposed ZrO_2 surfaces (cf. Figure S2).

The observation of water in IBA characterization (which is conducted in high vacuum) suggests that this physisorbed water is very strongly bound to the surface and might persist in atmospheric pressure conditions at high temperatures. An order of magnitude estimate of the thermodynamic driving force to desorption shows that the ΔG of evaporation of water at 900 °C should be approximately −155 kJ/mol. On the other hand, if the adsorbed water is capable of decreasing surface energy even by 0.01 J/m^2, the ΔG opposing desorption would be still 3 orders of magnitude larger (580 MJ/mol).

The amount of water that we extrapolate from the data from the samples *before* plasma processing (10% and 9%, respectively, for the TOPO and OA samples) is also noteworthy. This result is consistent with our previous characterizations[96] and with other reports:[114] nevertheless, the apparently ubiquitous presence of water in ligand shells of CNAs, most likely located at the core's surface where the polar groups of the ligands are found, is not quite widely recognized.

Interestingly, the data show that phosphorus is also observed in the OA samples, indicating that, in spite of the FT-IR results in Figure 2b that suggest nearly complete removal of the TOPO ligands, a small amount of TOPO is still bound to the particles.

To summarize this section, particles capped with TOPO and OA lead to remarkably similar CNAs, from which the organic elements of the ligands can be effectively removed by O_2 plasma processing. Trace amounts of inorganic compounds (e.g., the P in the ligands) are preserved and control the interfaces in between the crystalline cores in the CNA. Specifically, the TOPO-capped particles become capped by a phosphate-like shell. The CNAs after ligand removal are saturated with water, consistent with the increased pore space, the increased surface energy, and the small pore size (∼2 nm or less).

Growth Kinetics and Thermal Stabilization. Zirconium oxide is a high temperature ceramic widely used as a thermal barrier coating in gas turbines and jet engines due to its low thermal conductivity and as solid electrolyte in solid oxide fuel cells and as oxygen sensors due to its excellent oxygen ion conduction.

To stabilize ZrO_2 at high temperatures and prevent its phase transition to the monoclinic phase, the tetragonal phase is stabilized at room temperature by doping (e.g., with Y). Another approach to stabilization involves the reduction in size of the crystals in order to increase the surface area. The tetragonal phase has a significantly lower surface energy (1.02 J/m^2) than the monoclinic phase (1.52 J/m^2): as the crystal size decreases, the surface area per unit volume increases, leading to a relative stabilization of the tetragonal phase with respect to the monoclinic phase. Using basic thermodynamics and the tabulated thermochemical values for ZrO_2, it is possible to calculate that, at room temperature, ZrO_2 crystals smaller than 8.8 nm will be thermodynamically stable in the tetragonal phase (see the Supporting Information). The challenge of stabilizing ZrO_2 by size is to reduce crystal growth kinetics so that the high area of the interfaces is preserved throughout the operation of the material.

To understand the effect of the surface modification on the growth kinetics, we sintered plasma processed TOPO and OA samples and monitor the grain size as a function of time and temperature (Figure 3a). The particle sizes were determined by Scherrer analysis of the XRD spectrum, fitting the most intense and isolated reflection in the spectrum ((111) reflection at 30.2°) with a Gaussian curve (R^2 ranged between 0.98 and 0.99). The fwhm of the peak was then used as the measure of peak breadth. We assumed the particles to be spherical and used the appropriate Scherrer constant (K = 0.829).[115] The obtained crystallite size was further corrected to account for the spherical shape of the crystals, as described previously.[116] The average error in the average size determination (i.e., 95% confidence interval, delimited by shaded areas in Figure 3a) was 7% but was slightly higher for the smallest and largest particles due to the decreased accuracy of the fit.

The growth curves show a phenomenologically common trend with a rather steep increase in particle size in the first hour of sintering, followed by a quite sudden plateau. Qualitatively, the curves suggest that TOPO samples exhibit a rather slower growth, overall, whereas, on the other hand, they display a slightly faster growth at long sintering times. The data was quite accurately described (R^2 = 0.99 and 0.98 for TOPO and OA data sets, respectively) by an Ostwald ripening growth model[117−122] of the form $D(t) = D(t = 0) + kt^{1/n}$, where D is the diameter of the particles, k is the rate constant that should display an Arrhenius dependence on temperature, and n is the growth exponent that depends on the rate limiting process of growth (n = 2 indicates control by diffusion of ions at the matrix/particle interface, n = 3 indicates control by volume diffusion through the matrix, and n = 4 indicates control by dissolution kinetics[117]).

The model describes the experimental data significantly better than other models we used (e.g., growth models with variable exponents,[123] models accounting for impeded growth,[124] and models considering nonclassical crystallization processes[117]), and has fewer fitting parameters than most.

The fit of the growth kinetic curves was performed by constraining n to be dependent only on the surface chemistry of the particles. The samples exhibited a growth parameter of 2.28 ± 0.27 for TOPO samples, and 3.8 ± 1.2 for OA samples (in both cases, the error is the 95% confidence interval). According to the standard interpretation of the Ostwald ripening model,[117] these significantly different exponents would indicate that the rate limiting process in TOPO samples is diffusion of ions on the particle surface, whereas, in OA samples, it is the rate at which surface atoms become mobile. Both of these interpretations would be consistent with the presence of a phosphate layer in the TOPO samples that could hinder surface diffusion. On the other hand, caution in the interpretation is imperative for the following reasons: (i) Ostwald ripening is better suited and was originally formulated to describe ripening of particles in dilute solutions,[125] as the description by mean field theory of high filling fractions is analytically intractable and diffusion in highly confined systems is often anomalous; (ii) the molar excess Gibbs free energy of the surface changes significantly with size at these particle sizes and is expected to affect activation energies of growth. Nonetheless, the rate constants do follow an Arrhenius dependence on temperature (cf. Figure 3b). Qualitatively, the data suggest that the activation energy for growth of the TOPO samples is significantly larger than that for the OA samples. The fit yields activation energies that are significantly different from each other (111 ± 13 kJ/mol for TOPO and 48 ± 26 kJ/mol for OA), much smaller than commonly reported values for microcrystalline ZrO_2 (289−340 kJ/mol),[126,127] but closer to the values reported on nanocrystalline ZrO_2 (188−226 kJ/

DOI: 10.1021/acs.chemmater.7b02769
Chem. Mater. 2017, 29, 7888−7900

mol).[124] While these works reported nanocrystalline doped ZrO_2, the average sizes of their nanocrystals were >20 nm, whereas all our nanocrystals are approximately 1 order of magnitude smaller. It is understood that grain growth activation energies should decrease with decreasing grain size.[124]

The more rapid growth rate in OA samples is manifested in a different dependence of the porosity on the grain size and the sintering temperature (cf. Figure 3c—the data shown are for sintering times of 24 h). The porosity was estimated by assuming that the density of the solid phases in the CNAs remains constant, that the CNAs do not crack, and that none of the solid phases evaporate during sintering. Under such assumptions, the porosity of the films could be calculated from the knowledge of the porosity of the plasma processed films, and the shrinkage of the CNAs in the vertical direction.

The dependence of porosity on grain size is significantly different for the TOPO and OA samples (Figure 3c, left panel). The left panel of Figure 3c shows the change in porosity as a function of the diameter of the grains normalized against the initial grain size. Qualitatively, the two different interfaces lead to significantly different behaviors. In both cases, the porosity drops very significantly before any significant grain growth occurs. Interestingly, the consolidation occurring before grain growth is nearly the same for both types of samples (17% for OA and 16% for TOPO). This initial consolidation might be due, at least in part, to the desorption of adventitious contaminants (e.g., carbonates and water). After the initial drop, the two types of samples behave remarkably differently. The TOPO samples show a power law dependence (R^2 = 0.96 vs 0.86 for an exponential fit) on grain size of the form $P \propto D^{-\alpha}$, where P is the pore fraction and α is the exponent. This dependence is commonly observed in the consolidation of ceramics and is often attributed to pore-mediated growth.[123] Nonetheless, the exponent has an unusually large value of 0.45 ± 0.03 (as compared to the more commonly observed values of 0.2−0.3). The OA sample instead shows what could be an exponential decrease in porosity with grain size (R^2 = 0.998 vs 0.96 for a power law fit) with an exponent of −0.305 ± 0.007. This trend suggests that the process of consolidation (just like the growth mechanism, as discussed above) in the two types of samples is mechanistically different.

The remarkable reduction in growth kinetics obtained by controlling the interface chemistry of the particles resulted in a growth stabilization of the t-ZrO_2 phase that is comparable to that obtained by doping. Figure 3d shows the normalized grain size as a function of the sintering temperature for different types of nanocrystalline samples. The blue empty triangles show data from nanoparticles of Y-stabilized ZrO_2 (D = 3.7 nm) and their growth after 1 h of exposure to different sintering temperatures.[128] The black squares and red circles show, respectively, the data from the TOPO and OA samples after 2 h of exposure to the same range of temperatures. The OA samples show some initial grain growth at a temperature of 500 °C, whereas the TOPO samples remain essentially unchanged until 700 °C. Even though our samples had been sintered for an extra hour, the grain growth observed in our TOPO samples is significantly smaller than that shown by YSZ nanoparticles. Goto et al. also looked at the grain growth of t-ZrO_2 particles synthesized by a reaction analogous to the one used here but using oleylamine as a ligand rather than TOPO.[128] The particle size they obtain was similar. The grain growth of those particles as a function of sintering temperature is shown in Figure 3d in the open orange triangles. The faster growth, especially compared to our OA samples (whose surface should be comparably similar), is striking. We speculate that the increased growth rate resulted from the sintering of the samples prior to the removal of the ligands. As will be shown in a separate publication, the calcination of nanostructured materials in O_2 atmospheres does not come close to removing the carbon, which instead is left behind as amorphous carbon.[129] It is conceivable that the carbon matrix formed by the carbonization of the ligands could facilitate the growth of the nanoparticles.

The remarkable effect of such a minute change of the grain boundary composition on the growth kinetics is further accompanied by a very significant effect on the stabilization of the tetragonal phase. Figure 4a,b shows the Raman scattering from the CNAs of TOPO and OA samples at different stages of their processing and different sintering temperatures. For convenience, we have marked the frequencies of the vibrational modes of the tetragonal and monoclinic phases of ZrO_2 with green and blue vertical lines, respectively. The plots show quite clearly that the monoclinic phase appears in TOPO samples certainly when exposed to 900 °C (and maybe even at 800 °C). On the other hand, the OA samples show no obvious evidence of monoclinic phase at any temperature we tested. The difference in phase stabilization is noticeable even in the XRD characterization, at least in the samples sintered at 900 °C for 48 h (cf. Figure 4c): the TOPO samples show clear evidence of peaks at 28.2° and 31.5°, which are indicative of the monoclinic phase. The difference in thermal stability is not easily attributable to anything other than grain boundary composition. As previously discussed, the major factor in controlling the relative thermodynamic stability of the two phases is the surface area per unit volume and the molar surface energy. The surface area is expected to be similar since the average particle size for the samples sintered at 900 °C for 48 h was 21.10 ± 1.81 nm and 23.29 ± 0.61 nm for the TOPO and OA samples, respectively. The error indicates the 95% confidence interval on the value of the average size, but we expect that the polydispersity to be at least as large as the one found in the starting nanoparticles (6% and 8% or 1.3 and 1.9 nm). Therefore, the size distributions overlap very significantly.

In summary, while the phosphate groups at the grain boundary appear to significantly slow down grain growth, they might facilitate the phase transition to the monoclinic phase. (It is important to notice that all the sintered samples that showed t-ZrO_2 grain sizes larger than 10 nm are most likely not thermodynamically stable at room temperature and therefore that the stabilization of the tetragonal phase in those samples is most likely due to kinetic factors rather than thermodynamic, e.g., surface energy.)

Interfacial Energies and Mechanical Properties. The slower growth kinetics in TOPO samples can be hypothesized to originate from a decrease in the interfacial energy (γ = 1.02 J/m^2 for t-ZrO_2 and ranges between 0.15 and 0.35 J/m^2 for reported phosphates), as well as by a reduction on grain boundary mobility caused by the phosphate groups. We therefore used nanoindentation to measure the Young's modulus and hardness of the CNA before and after sintering. The mechanical properties in polycrystalline ceramics as well as granular materials are heavily influenced by the composition of the grain boundary.

The modulus of the films, corrected for the influence of the substrate,[130] was found to be strongly dependent on the sintering temperatures. Our previous work[96] has shown that the modulus of ligand-capped as well as ligand-free CNAs can be

DOI: 10.1021/acs.chemmater.7b02769
Chem. Mater. 2017, 29, 7888−7900

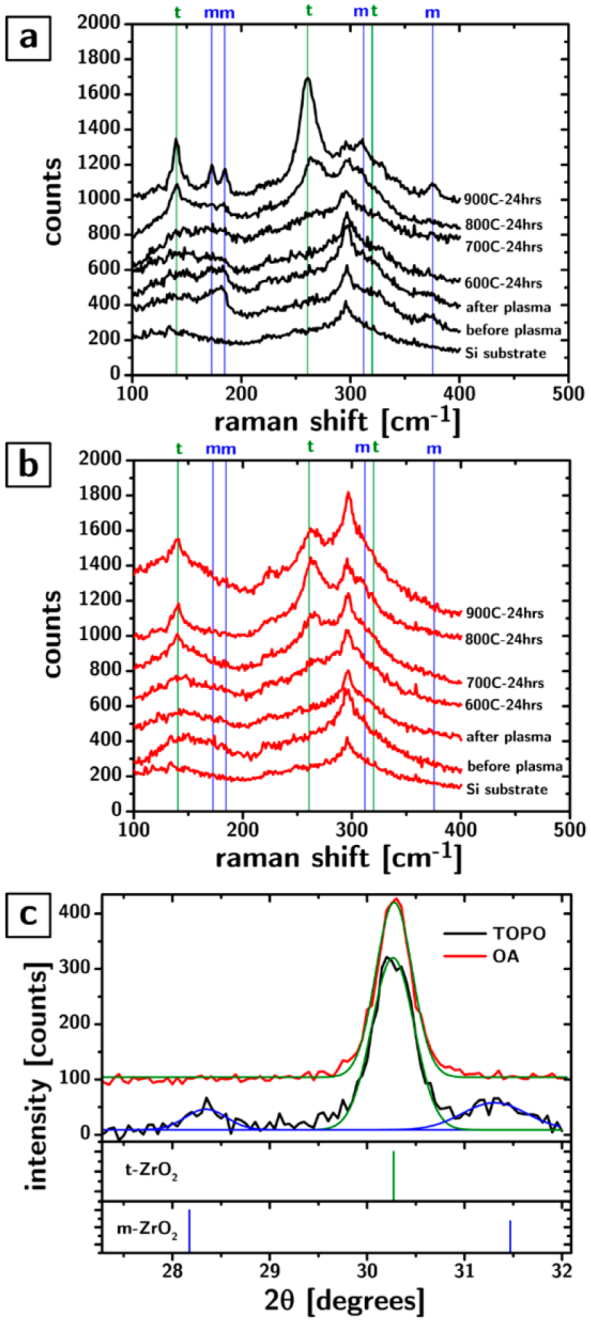

Figure 4. Thermal stability of the tetragonal phase as affected by interface composition. Raman scattering of TOPO (a) and OA (b) films before and after plasma processing and after sintering at different temperatures for 24 h. (c) XRD characterization of TOPO and OA films sintered at 900 °C for 48 h showing the appearance (in the case of TOPO samples) or lack thereof (in the case of OA samples) of the monoclinic phase. The curves show Gaussian fits of the diffraction peaks.

quantitatively predicted by the granular model by Kendall et al.[131] that accounts for the effects of porosity φ, grain size D, bulk modulus E_b, and interface energy Γ according to the following equation

$$E = 17.1\varphi^4\left[\frac{\Gamma E_b^2}{D}\right]^{1/3}$$

To understand whether the same model could be applied in sintered CNAs, we plotted the experimental moduli against $\zeta = \frac{\varphi^4}{D^{1/3}}$. If the model is valid, assuming that the interfacial energy is independent of temperature, the plot of $E(\zeta)$ (cf. Figure 5a) should be describable by a straight line through the origin $E(\zeta) = \beta\cdot\zeta$, whose slope β is equal to $17.1E_b^{2/3}\Gamma^{1/3}$. The linear fit is adequate (R^2 = 0.98 and 0.99), especially considering the associated experimental errors. The fit is especially good for the OA samples, which is interesting and unexpected. The data originate from samples that have undergone, especially at high temperature, significant grain growth. It is not intuitive to describe the material as a granular system. On the other hand, the mechanical properties were determined by substrate-corrected indentation, using a Berkovich indenter. It is assumed that, in these conditions, the deformation of the material is plastic. It is conceivable that, in these conditions, the grains in the polycrystal could still be described as grains in a granular system. What is further surprising is the extent of agreement with the model, considering that it was developed under the assumption of spherical grains.

From the slope, we can calculate the values of interfacial energy (and therefore the values of surface energy assuming that $\Gamma = 2\cdot\gamma$, which is fair since we are dealing with a homogeneous unary system), if we assume that the bulk energy is constant throughout the data set. This assumption is valid for all samples sintered at temperatures lower than 900 °C, and even for those sintered at 900 °C, the conversion of the TOPO samples to monoclinic is small. The values of surface energy are 0.04 ± 0.01 and 0.11 ± 0.02 J/m^2 for the TOPO and OA samples, respectively. These values are not consistent with the expected surface energies of the bare solid phases (0.1−0.3 J/m^2 for phosphates and 1.02 J/m^2 for t-ZrO_2), but they are consistent with the presence of water in between the grains due to adsorption from the atmosphere and capillary condensation, as already observed by Kendall.[131]

Using the fitted values of surface energy from Figure 5a, the modulus data as a function of temperature for both TOPO and OA samples can be qualitatively reproduced by the Kendall model (Figure 5b). Using the same assumptions used in our previous work,[96] the model allows us to also predict the modulus of the as-deposited (data shown for comparison in Figure 5b at T = 0 °C) and plasma treated samples (data shown, for comparison in Figure 5b at T = 25 °C). In summary, these assumptions are that the bulk modulus and surface energy of the unprocessed CNA should be equal to that of the ligands.

The modulus of the TOPO samples before sintering is 53 GPa, which is similar to the values we previously reported for similar samples[96] (45 GPa), whereas, for OA samples, the modulus is significantly smaller at 35 GPa. According to the model, the difference in modulus is accounted for by the higher porosity of the plasma processed OA samples, which we discussed before. Due to their higher growth rate, the porosity of the OA samples decreases faster than that of the TOPO samples and they become similar at high sintering temperatures, resulting in similar maximum moduli (the difference in surface energy between OA and TOPO samples is a minor influence compared to the differences in porosity: according to Kendall's model, the modulus scales with the fourth power of the porosity but only as the cube root of the surface energy).

The data in Figure 5b show that the maximum modulus achieved (92 ± 9 and 91 ± 5 GPa for TOPO and OA samples)

DOI: 10.1021/acs.chemmater.7b02769
Chem. Mater. 2017, 29, 7888−7900

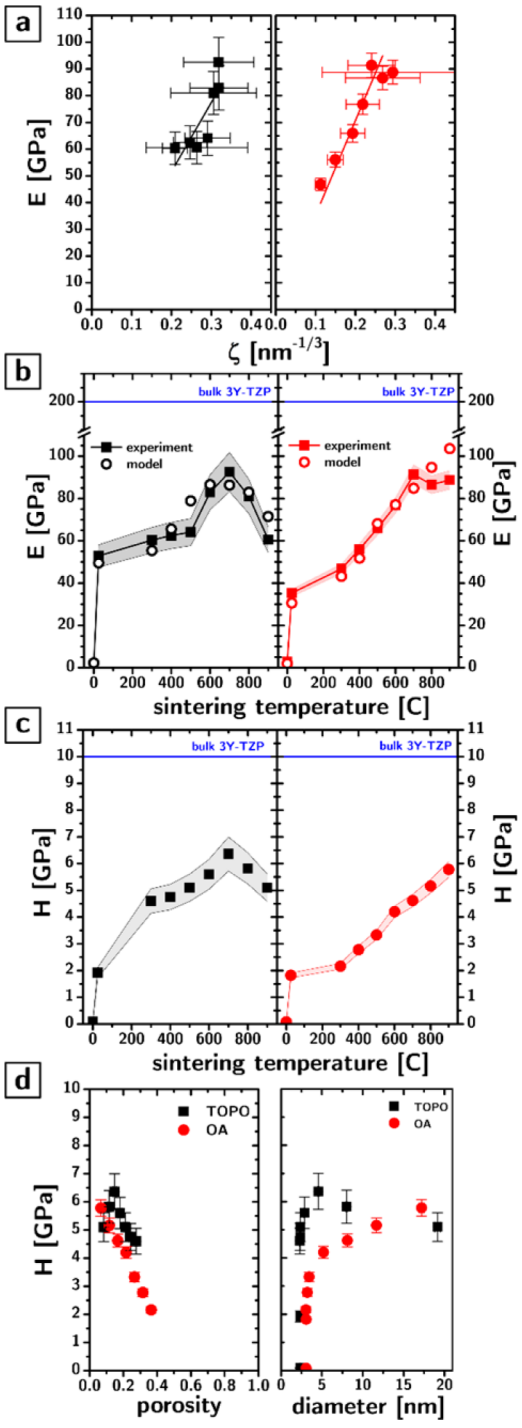

Figure 5. Influence of interface composition on mechanical properties. (a) Dependency of experimentally determined modulus of TOPO (left) and OA (right) samples on the ζ parameter. The linear dependence indicates the compatibility of the data with Kendall's granular model. (b) Experimental moduls (square scatters) for TOPO (left) and OA (right) samples as a function of the sintering temperature. The open scatters indicate the prediction of the Kendall model based on the interfacial energies determined from the slopes in panel (a). (c) Hardness as a function of sintering temperature for TOPO (left) and OA (right) samples. (d) Hardness as a function of porosity (left) and grain size (right) for TOPO (black squares) and OA (red circles) samples. In all the above panels, shaded areas behind data points identify the 95% confidence interval on the average value.

is nearly half of the single crystal bulk modulus of 200 GPa and occurs at the intermediate sintering temperature of 700 °C. The drop in modulus at higher sintering temperatures for TOPO samples results from the growth in grain size outweighing the rather small decrease in porosity, thereby creating a maximum. In the case of OA samples, the discrepancy at high sintering temperatures could very well be a result of the error in the determination of porosity: at such small porosities (<10%), a 1% error leads to a very significant change in the predicted modulus. Another possibility for the discrepancies at high temperatures could be that the Kendall model fails to describe the system: the high modulus data are the ones that show the greatest discrepancy from the model in Figure 5a.

The hardness of the CNAs is also significantly improved by sintering. The plasma-processed TOPO samples show a hardness of 1.92 GPa, which is consistent with the value reported in our previous work for similar samples (2.2 GPa). Sintering causes the hardness to increase up to 6.36 GPa at 700 °C and then decrease at higher temperatures. This hardness is quite remarkable as it is 64% of the single crystal hardness (10 GPa). The OA samples instead show a significantly smaller hardness throughout the sintering range, in spite of similar porosity at high sintering temperatures (Figure 5c). The hardness of the OA samples is lower at low temperatures because the porosity is higher (30−40% instead of 20−30% for TOPO) and, maybe, because the particles are slightly bigger. Furthermore, the phosphate termination of the interfaces in the TOPO samples could be contributing to the hardening of the material. At the highest temperatures, the hardness of the OA samples catches up to that of the TOPO samples because the TOPO sample's hardness decreases (mostly due, in our opinion, to the increasing monoclinic fraction) while the OA samples keep increasing (these samples do not convert to the monoclinic phase and have, at those temperatures, similar porosity).

It is important to try and detangle the role of particle size, porosity, and surface chemistry on the hardness of these nanocrystalline ceramics. While it might appear difficult to do so for a sintering series like this in which all parameters are dependent on each other, an analysis of the individual dependencies is possible and instructive. The dependence of hardness on porosity for TOPO and OA sintered samples is shown in Figure 5d. At higher porosities, the samples follow what appears to be a linear increase in hardness with decreasing porosity. The slope is similar for both the TOPO and OA samples (-13.7 ± 2.1 vs 12.3 ± 0.5 GPa). The intercepts are, nonetheless, significantly different (8.1 ± 0.4 vs 6.7 ± 0.1 GPa), indicating that, for equal porosity, the TOPO samples are harder than the OA samples (strongly suggestive of the role of interfacial composition on hardening of the material). At low porosities (i.e., high sintering temperatures), the TOPO samples show a decrease in hardness with a decrease in porosity, which could be explained by a particle size dependence of hardness (which is though not observed in the OA series) or more simply by the formation of a softer monoclinic phase which is peculiar to TOPO samples and indeed start forming at the temperatures at which the hardness starts decreasing.

As shown in Figure 5d, the dependence of hardness on grain size is also strikingly different for the two types of interfaces. In the case of OA samples, the increase in the hardness with increasing grain size can be entirely ascribed to the decrease in porosity as the grain size increases. In the case of TOPO

DOI: 10.1021/acs.chemmater.7b02769
Chem. Mater. 2017, 29, 7888−7900

samples, the increase in hardness with particle size is reversed above 5 nm and could be ascribed in part to the development of the monoclinic phase.

CONCLUSIONS

In this work, we have described a methodology to create nanostructured, all-inorganic materials with a selective control of the composition of the solid/solid interfaces inside them. The approach takes colloidal nanocrystals capped with ligands, deposits them as a solid composed of inorganic cores and ligands, and then uses plasma processing to selectively react with the ligands. We demonstrate here that this materials synthesis approach allows controlling the composition of the interfaces by controlling the composition of the ligand shell. Specifically, using ligands containing inorganic elements and using feed gases that do not produce volatile compounds by reacting with those elements (e.g., O_2 plasma on P-containing ligands), leaves behind groups (e.g., phosphate) that modify the chemical composition of the surfaces the ligands were bound to. The advantage of this approach is that, by controlling the composition and structure of the ligand, or by using mixtures of ligands, one could envision developing sophisticated control of the solid/solid interface compositions inside ligand-free nanocrystal superlattices, with potentially important effects on mechanical, transport, magnetic, and optical properties.

This work focused on t-ZrO_2 nanoparticles capped with oleic acid and trioctylphosphine oxide. The particles were deposited as films, and the organic components of their ligands were removed by plasma etching. Analysis of these materials and of their properties led us to the following conclusions.

The O_2 plasma processing of TOPO ligands leads to the formation of phosphate groups. The low temperature of the processing (~40−50 °C) and the characterization of the material by IBA suggest that the phosphorus species are not displaced. OA ligands instead left no trace on the nanoparticles that could not be attributed to adventitious contamination.

The plasma-processed, ligand-free films are porous and entirely filled with water. The small size of the pores in the material (<2 nm) is consistent with extensive capillary condensation in common relative humidities. Due to the large surface area and small pore size, the large amount of water is consistent with the deposition of a single monolayer of water on the particle surfaces.

The different interface compositions of the materials lead to changes in the grain growth kinetics at high temperature, phase stabilization, and mechanical properties. Specifically, the growth kinetics of the samples could be described by an Ostwald ripening model. The growth exponents were significantly different for the two interface chemistries and indicative of different rate limiting processes of growth. The activation energies were also found to be significantly different, with phosphate-coated surfaces showing a higher activation energy of growth. All activation energies were found to be substantially smaller than previously reported for similar phases with larger grain size, suggesting a strong dependence of grain growth activation energies for grain size below 10 nm. The increased activation energy for growth associated with the interfacial phosphates made the samples significantly more thermally stable than state-of-the-art nanostructured YSZ (with no detectable coarsening at temperatures as high as 600 °C). The phase transformation from tetragonal phase to the monoclinic phase was also affected by the interface composition with phosphate interfaces seemingly facilitating the conversion to monoclinic phase.

The modulus of the films could be described in all cases with a granular model. The surface energies extracted from the model indicate that interfacial phosphate significantly reduces the interfacial energy, consistent with the slower grain growth kinetics.

ASSOCIATED CONTENT

Supporting Information

The Supporting Information is available free of charge on the ACS Publications website at DOI: 10.1021/acs.chemmater.7b02769.

Materials & methods, supporting discussion of the volume fractions determinations, XPS spectrum of the Zr 3d line, FT-IR characterization of the plasma processed TOPO and OA samples, ΔG of transition from the monoclinic to the tetragonal phase as a function of crystal diameter, and load vs displacement curves for the sintered films (PDF)

AUTHOR INFORMATION

Corresponding Author

*E-mail: lcademar@iastate.edu.

ORCID

Emily A. Smith: 0000-0001-7438-7808

Ludovico Cademartiri: 0000-0001-8805-9434

Notes

The authors declare no competing financial interest.

ACKNOWLEDGMENTS

The work described in this paper has been supported by the Member-Specific-Research-Intel program of Semiconductor Research Corporation under Award No. 2015-IN-2582. The authors thank Dapeng Jing for his assistance with X-ray photoelectron spectroscopy. The Raman measurements were supported by the U.S. Department of Energy, Office of Basic Energy Sciences, Division of Chemical Sciences, Geosciences, and Biosciences through the Ames Laboratory. The Ames Laboratory is operated for the U.S. Department of Energy by Iowa State University under Contract No. DE-AC02-07CH11358.

REFERENCES

(1) Bernevig, B. A.; Hughes, T. L.; Zhang, S. C. Quantum spin hall effect and topological phase transition in hgte quantum wells. *Science* **2006**, *314*, 1757−1761.

(2) Hasan, M. Z.; Kane, C. L. Colloquium: Topological insulators. *Rev. Mod. Phys.* **2010**, *82*, 3045−3067.

(3) Zhang, H. J.; Liu, C. X.; Qi, X. L.; Dai, X.; Fang, Z.; Zhang, S. C. Topological insulators in bi2se3, bi2te3 and sb2te3 with a single dirac cone on the surface. *Nat. Phys.* **2009**, *5*, 438−442.

(4) Bert, J. A.; Kalisky, B.; Bell, C.; Kim, M.; Hikita, Y.; Hwang, H. Y.; Moler, K. A. Direct imaging of the coexistence of ferromagnetism and superconductivity at the laalo3/srtio3 interface. *Nat. Phys.* **2011**, *7*, 767−771.

(5) Hwang, H. Y.; Iwasa, Y.; Kawasaki, M.; Keimer, B.; Nagaosa, N.; Tokura, Y. Emergent phenomena at oxide interfaces. *Nat. Mater.* **2012**, *11*, 103−113.

(6) Mannhart, J.; Schlom, D. G. Oxide interfaces-an opportunity for electronics. *Science* **2010**, *327*, 1607−1611.

(7) Reyren, N.; Thiel, S.; Caviglia, A. D.; Kourkoutis, L. F.; Hammerl, G.; Richter, C.; Schneider, C. W.; Kopp, T.; Ruetschi, A. S.; Jaccard,

DOI: 10.1021/acs.chemmater.7b02769
Chem. Mater. 2017, 29, 7888−7900

D.; Gabay, M.; Muller, D. A.; Triscone, J. M.; Mannhart, J. Superconducting interfaces between insulating oxides. *Science* **2007**, *317*, 1196−1199.
(8) Geim, A. K.; Novoselov, K. S. The rise of graphene. *Nat. Mater.* **2007**, *6*, 183−191.
(9) Novoselov, K. S.; Geim, A. K.; Morozov, S. V.; Jiang, D.; Zhang, Y.; Dubonos, S. V.; Grigorieva, I. V.; Firsov, A. A. Electric field effect in atomically thin carbon films. *Science* **2004**, *306*, 666−669.
(10) Roduner, E. *Nanoscopic Materials: Size Dependent Phenomena*; Royal Society of Chemistry: Cambridge, U.K., 2006.
(11) Cademartiri, L.; Ozin, G. A. *Concepts of Nanochemistry*; Wiley-VCH: Weinheim, 2009.
(12) Wenzel, R. N. Resistance of solid surfaces to wetting by water. *Ind. Eng. Chem.* **1936**, *28*, 988−994.
(13) Lafuma, A.; Quere, D. Superhydrophobic states. *Nat. Mater.* **2003**, *2*, 457−460.
(14) Tuteja, A.; Choi, W.; Ma, M. L.; Mabry, J. M.; Mazzella, S. A.; Rutledge, G. C.; McKinley, G. H.; Cohen, R. E. Designing superoleophobic surfaces. *Science* **2007**, *318*, 1618−1622.
(15) Wong, T. S.; Kang, S. H.; Tang, S. K. Y.; Smythe, E. J.; Hatton, B. D.; Grinthal, A.; Aizenberg, J. Bioinspired self-repairing slippery surfaces with pressure-stable omniphobicity. *Nature* **2011**, *477*, 443−447.
(16) Diebold, U. The surface science of titanium dioxide. *Surf. Sci. Rep.* **2003**, *48*, 53−229.
(17) Fujishima, A.; Zhang, X. T.; Tryk, D. A. Tio2 photocatalysis and related surface phenomena. *Surf. Sci. Rep.* **2008**, *63*, 515−582.
(18) Somorjai, G. A.; Frei, H.; Park, J. Y. Advancing the frontiers in nanocatalysis, biointerfaces, and renewable energy conversion by innovations of surface techniques. *J. Am. Chem. Soc.* **2009**, *131*, 16589−16605.
(19) Somorjai, G. A.; Park, J. Y. Molecular factors of catalytic selectivity. *Angew. Chem., Int. Ed.* **2008**, *47*, 9212−9228.
(20) Yamada, Y.; Tsung, C. K.; Huang, W.; Huo, Z. Y.; Habas, S. E.; Soejima, T.; Aliaga, C. E.; Somorjai, G. A.; Yang, P. D. Nanocrystal bilayer for tandem catalysis. *Nat. Chem.* **2011**, *3*, 372−376.
(21) Atwater, H. A.; Polman, A. Plasmonics for improved photovoltaic devices. *Nat. Mater.* **2010**, *9*, 205−213.
(22) Ozbay, E. Plasmonics: Merging photonics and electronics at nanoscale dimensions. *Science* **2006**, *311*, 189−193.
(23) Schuller, J. A.; Barnard, E. S.; Cai, W. S.; Jun, Y. C.; White, J. S.; Brongersma, M. L. Plasmonics for extreme light concentration and manipulation. *Nat. Mater.* **2010**, *9*, 193−204.
(24) Stiles, P. L.; Dieringer, J. A.; Shah, N. C.; Van Duyne, R. R. Surface-enhanced raman spectroscopy. *Annu. Rev. Anal. Chem.* **2008**, *1*, 601−626.
(25) Love, J. C.; Estroff, L. A.; Kriebel, J. K.; Nuzzo, R. G.; Whitesides, G. M. Self-assembled monolayers of thiolates on metals as a form of nanotechnology. *Chem. Rev.* **2005**, *105*, 1103−1169.
(26) Ulman, A. Formation and structure of self-assembled monolayers. *Chem. Rev.* **1996**, *96*, 1533−1554.
(27) Bhushan, B.; Israelachvili, J. N.; Landman, U. Nanotribology - friction, wear and lubrication at the atomic-scale. *Nature* **1995**, *374*, 607−616.
(28) Urbakh, M.; Klafter, J.; Gourdon, D.; Israelachvili, J. The nonlinear nature of friction. *Nature* **2004**, *430*, 525−528.
(29) Wang, C.; Hu, Y.; Lieber, C. M.; Sun, S. Ultrathin au nanowires and their transport properties. *J. Am. Chem. Soc.* **2008**, *130*, 8902−8903.
(30) Dresselhaus, M. S.; Dresselhaus, G.; Sun, X.; Zhang, Z.; Cronin, S. B.; Koga, T.; Ying, J. Y.; Chen, G. The promise of low-dimensional thermoelectric materials. *Microscale Thermophys. Eng.* **1999**, *3*, 89−100.
(31) Minnich, A. J.; Dresselhaus, M. S.; Ren, Z. F.; Chen, G. Bulk nanostructured thermoelectric materials: Current research and future prospects. *Energy Environ. Sci.* **2009**, *2*, 466−479.
(32) Kumar, K. S.; Van Swygenhoven, H.; Suresh, S. Mechanical behavior of nanocrystalline metals and alloys. *Acta Mater.* **2003**, *51*, 5743−5774.
(33) Meyers, M. A.; Mishra, A.; Benson, D. J. Mechanical properties of nanocrystalline materials. *Prog. Mater. Sci.* **2006**, *51*, 427−556.
(34) Kahn, A.; Koch, N.; Gao, W. Y. Electronic structure and electrical properties of interfaces between metals and pi-conjugated molecular films. *J. Polym. Sci., Part B: Polym. Phys.* **2003**, *41*, 2529−2548.
(35) Rashba, E. I. Theory of electrical spin injection: Tunnel contacts as a solution of the conductivity mismatch problem. *Phys. Rev. B: Condens. Matter Mater. Phys.* **2000**, *62*, R16267−R16270.
(36) Wang, Q.; Moser, J. E.; Gratzel, M. Electrochemical impedance spectroscopic analysis of dye-sensitized solar cells. *J. Phys. Chem. B* **2005**, *109*, 14945−14953.
(37) Dinega, D. P.; Bawendi, M. G. A solution-phase chemical approach to a new crystal structure of cobalt. *Angew. Chem., Int. Ed.* **1999**, *38*, 1788−1791.
(38) Joo, J.; Yu, T.; Kim, Y. W.; Park, H. M.; Wu, F. X.; Zhang, J. Z.; Hyeon, T. Multigrarn scale synthesis and characterization of monodisperse tetragonal zirconia nanocrystals. *J. Am. Chem. Soc.* **2003**, *125*, 6553−6557.
(39) Hall, E. O. The deformation and ageing of mild steel: Iii discussion of results. *Proc. Phys. Soc., London, Sect. B* **1951**, *64*, 747.
(40) Petch, N. J. The cleavage strength of polycrystals. *J. Iron Steel Inst. London* **1953**, *174*, 25−28.
(41) Karch, J.; Birringer, R.; Gleiter, H. Ceramics ductile at low-temperature. *Nature* **1987**, *330*, 556−558.
(42) Waku, Y.; Nakagawa, N.; Wakamoto, T.; Ohtsubo, H.; Shimizu, K.; Kohtoku, Y. A ductile ceramic eutectic composite with high strength at 1,873 k. *Nature* **1997**, *389*, 49−52.
(43) Kim, J. K.; Mai, Y. W. High-strength, high fracture-toughness fiber composites with interface control - a review. *Compos. Sci. Technol.* **1991**, *41*, 333−378.
(44) Valiev, R. Z.; Estrin, Y.; Horita, Z.; Langdon, T. G.; Zechetbauer, M. J.; Zhu, Y. T. Producing bulk ultrafine-grained materials by severe plastic deformation. *JOM* **2006**, *58*, 33−39.
(45) Balluffi, R. W.; Allen, S.; Carter, W. C. *Kinetics of Materials*; John Wiley & Sons: Hoboken, NJ, 2005.
(46) Kirchheim, R. Reducing grain boundary, dislocation line and vacancy formation energies by solute segregation. I. Theoretical background. *Acta Mater.* **2007**, *55*, 5129−5138.
(47) Chookajorn, T.; Murdoch, H. A.; Schuh, C. A. Design of stable nanocrystalline alloys. *Science* **2012**, *337*, 951−954.
(48) Sun, S. H.; Zeng, H.; Robinson, D. B.; Raoux, S.; Rice, P. M.; Wang, S. X.; Li, G. X. Monodisperse mfe2o4 (m = fe, co, mn) nanoparticles. *J. Am. Chem. Soc.* **2004**, *126*, 273−279.
(49) Hyeon, T. Chemical synthesis of magnetic nanoparticles. *Chem. Commun.* **2003**, 927−934.
(50) Kwon, S. G.; Piao, Y.; Park, J.; Angappane, S.; Jo, Y.; Hwang, N. M.; Park, J. G.; Hyeon, T. Kinetics of monodisperse iron oxide nanocrystal formation by "heating-up" process. *J. Am. Chem. Soc.* **2007**, *129*, 12571−12584.
(51) Choi, S. H.; Na, H. B.; Park, Y. I.; An, K.; Kwon, S. G.; Jang, Y.; Park, M.; Moon, J.; Son, J. S.; Song, I. C.; Moon, W. K.; Hyeon, T. Simple and generalized synthesis of oxide-metal heterostructured nanoparticles and their applications in multimodal biomedical probes. *J. Am. Chem. Soc.* **2008**, *130*, 15573−15580.
(52) Yu, T.; Joo, J.; Park, Y. I.; Hyeon, T. Single unit cell thick samaria nanowires and nanoplates. *J. Am. Chem. Soc.* **2006**, *128*, 1786−1787.
(53) Yu, T. Y.; Joo, J.; Park, Y. I.; Hyeon, T. Large-scale nonhydrolytic sol-gel synthesis of uniform-sized ceria nanocrystals with spherical, wire, and tadpole shapes. *Angew. Chem., Int. Ed.* **2005**, *44*, 7411−7414.
(54) Tang, J.; Fabbri, J.; Robinson, R. D.; Zhu, Y.; Herman, I. P.; Steigerwald, M. L.; Brus, L. E. Solid-solution nanoparticles: Use of a nonhydrolytic sol-gel synthesis to prepare hfo2 and hfxzr1-xo2 nanocrystals. *Chem. Mater.* **2004**, *16*, 1336−1342.
(55) Joo, J.; Yu, T.; Kim, Y. W.; Park, H. M.; Wu, F.; Zhang, J. Z.; Hyeon, T. Multigram scale synthesis and characterization of

DOI: 10.1021/acs.chemmater.7b02769
Chem. Mater. 2017, 29, 7888−7900

monodisperse tetragonal zirconia nanocrystals. *J. Am. Chem. Soc.* **2003**, *125*, 6553−6557.
(56) Murray, C. B.; Norris, D. J.; Bawendi, M. G. Synthesis and characterization of nearly monodisperse cde (e = s, se, te) semiconductor nanocrystallites. *J. Am. Chem. Soc.* **1993**, *115*, 8706−8715.
(57) Hines, M. A.; Scholes, G. D. Colloidal pbs nanocrystals with size-tunable near-infrared emission. Observation of post-synthesis self-narrowing of the particle size distribution. *Adv. Mater.* **2003**, *15*, 1844−1849.
(58) Bakueva, L.; Musikhin, S.; Hines, M. A.; Chang, T. W. F.; Tzolov, M.; Scholes, G. D.; Sargent, E. H. Size-tunable infrared (1000−1600 nm) electroluminescence from pbs quantum-dot nanocrystals in a semiconducting polymer. *Appl. Phys. Lett.* **2003**, *82*, 2895−2897.
(59) Hines, M. A.; Guyot-Sionnest, P. Bright uv-blue luminescent colloidal znse nanocrystals. *J. Phys. Chem. B* **1998**, *102*, 3655−3657.
(60) Peng, X. G.; Schlamp, M. C.; Kadavanich, A. V.; Alivisatos, A. P. Epitaxial growth of highly luminescent cdse/cds core/shell nanocrystals with photostability and electronic accessibility. *J. Am. Chem. Soc.* **1997**, *119*, 7019−7029.
(61) Hines, M. A.; Guyot-Sionnest, P. Synthesis and characterization of strongly luminescing zns-capped cdse nanocrystals. *J. Phys. Chem.* **1996**, *100*, 468−471.
(62) Gaschler, W. L.; Murray, C. B.; Stokes, K. L. Synthesis and characterization of PbSe nanocrystal (quantum dot) superlattices. *Abstr. Pap.—Am. Chem. Soc.* **2000**, *219*, U582−U582.
(63) Cademartiri, L.; Guerin, G.; Bishop, K. J. M.; Winnik, M. A.; Ozin, G. A. Polymer-like conformation and growth kinetics of bi2s3 nanowires. *J. Am. Chem. Soc.* **2012**, *134*, 9327−9334.
(64) Cademartiri, L.; Ozin, G. A. Emerging strategies for the synthesis of highly monodisperse colloidal nanostructures. *Philos. Trans. R. Soc., A* **2010**, *368*, 4229−4248.
(65) Cademartiri, L.; Malakooti, R.; O'Brien, P. G.; Migliori, A.; Petrov, S.; Kherani, N. P.; Ozin, G. A. Large-scale synthesis of ultrathin bi2s3 necklace nanowires. *Angew. Chem., Int. Ed.* **2008**, *47*, 3814−3817.
(66) Cademartiri, L.; Bertolotti, J.; Sapienza, R.; Wiersma, D. S.; von Freymann, G.; Ozin, G. A. Multigram scale, solventless and diffusion-controlled route to highly monodisperse pbs nanocrystals. *J. Phys. Chem. B* **2006**, *110*, 671−673.
(67) Moreels, I.; Lambert, K.; Smeets, D.; De Muynck, D.; Nollet, T.; Martins, J. C.; Vanhaecke, F.; Vantomme, A.; Delerue, C.; Allan, G.; Hens, Z. Size-dependent optical properties of colloidal pbs quantum dots. *ACS Nano* **2009**, *3*, 3023−3030.
(68) Moreels, I.; Lambert, K.; De Muynck, D.; Vanhaecke, F.; Poelman, D.; Martins, J. C.; Allan, G.; Hens, Z. Composition and size-dependent extinction coefficient of colloidal pbse quantum dots. *Chem. Mater.* **2007**, *19*, 6101−6106.
(69) Battaglia, D.; Peng, X. Formation of high quality inp and inas nanocrystals in a noncoordinating solvent. *Nano Lett.* **2002**, *2*, 1027−1030.
(70) Tang, C.; Fan, S.; Lamy de la Chapelle, M.; Dang, H.; Li, P. Synthesis of gallium phosphide nanorods. *Adv. Mater.* **2000**, *12*, 1346−1348.
(71) Cao, Y.-W.; Aksenton, J.; Soloviev, V.; Banin, U. Colloidal synthesis and properties of inas/inp and inas/cdse core/shell nanocrystals. *MRS Online Proc. Libr.* **1999**, *571*, 75−80.
(72) Henkes, A. E.; Schaak, R. E. Trioctylphosphine: A general phosphorus source for the low-temperature conversion of metals into metal phosphides. *Chem. Mater.* **2007**, *19*, 4234−4242.
(73) Henkes, A. E.; Vasquez, Y.; Schaak, R. E. Converting metals into phosphides: A general strategy for the synthesis of metal phosphide nanocrystals. *J. Am. Chem. Soc.* **2007**, *129*, 1896−1897.
(74) Xu, S.; Ziegler, J.; Nann, T. Rapid synthesis of highly luminescent inp and inp/zns nanocrystals. *J. Mater. Chem.* **2008**, *18*, 2653−2656.
(75) Liu, W. Y.; Chang, A. Y.; Schaller, R. D.; Talapin, D. V. Colloidal insb nanocrystals. *J. Am. Chem. Soc.* **2012**, *134*, 20258−20261.
(76) Srivastava, V.; Liu, W. Y.; Janke, E. M.; Kamysbayev, V.; Filatov, A. S.; Sun, C. J.; Lee, B.; Rajh, T.; Schaller, R. D.; Talapin, D. V. Understanding and curing structural defects in colloidal gaas nanocrystals. *Nano Lett.* **2017**, *17*, 2094−2101.
(77) Andaraarachchi, H. P.; Thompson, M. J.; White, M. A.; Fan, H. J.; Vela, J. Phase-programmed nanofabrication: Effect of organophosphite precursor reactivity on the evolution of nickel and nickel phosphide nanocrystals. *Chem. Mater.* **2015**, *27*, 8021−8031.
(78) White, M. A.; Thompson, M. J.; Miller, G. J.; Vela, J. Got liznp? Solution phase synthesis of filled tetrahedral semiconductors in the nanoregime. *Chem. Commun.* **2016**, *52*, 3497−3499.
(79) Qian, H.; Zhu, M.; Wu, Z.; Jin, R. Quantum sized gold nanoclusters with atomic precision. *Acc. Chem. Res.* **2012**, *45*, 1470−1479.
(80) Halder, A.; Ravishankar, N. Ultrafine single-crystalline gold nanowire arrays by oriented attachment. *Adv. Mater.* **2007**, *19*, 1854−1858.
(81) Jones, M. R.; Osberg, K. D.; Macfarlane, R. J.; Langille, M. R.; Mirkin, C. A. Templated techniques for the synthesis and assembly of plasmonic nanostructures. *Chem. Rev.* **2011**, *111*, 3736−3827.
(82) Langille, M. R.; Personick, M. L.; Zhang, J.; Mirkin, C. A. Defining rules for the shape evolution of gold nanoparticles. *J. Am. Chem. Soc.* **2012**, *134*, 14542−14554.
(83) Millstone, J. E.; Hurst, S. J.; Metraux, G. S.; Cutler, J. I.; Mirkin, C. A. Colloidal gold and silver triangular nanoprisms. *Small* **2009**, *5*, 646−664.
(84) Pietrobon, B.; Kitaev, V. Photochemical synthesis of monodisperse size-controlled silver decahedral nanoparticles and their remarkable optical properties. *Chem. Mater.* **2008**, *20*, 5186−5190.
(85) Skrabalak, S. E.; Au, L.; Li, X. D.; Xia, Y. N. Facile synthesis of ag nanocubes and au nanocages. *Nat. Protoc.* **2007**, *2*, 2182−2190.
(86) Skrabalak, S. E.; Chen, J. Y.; Sun, Y. G.; Lu, X. M.; Au, L.; Cobley, C. M.; Xia, Y. N. Gold nanocages: Synthesis, properties, and applications. *Acc. Chem. Res.* **2008**, *41*, 1587−1595.
(87) Wiley, B. J.; Im, S. H.; Li, Z. Y.; McLellan, J.; Siekkinen, A.; Xia, Y. N. Maneuvering the surface plasmon resonance of silver nanostructures through shape-controlled synthesis. *J. Phys. Chem. B* **2006**, *110*, 15666−15675.
(88) Xia, Y. N.; Xiong, Y. J.; Lim, B.; Skrabalak, S. E. Shape-controlled synthesis of metal nanocrystals: Simple chemistry meets complex physics? *Angew. Chem., Int. Ed.* **2009**, *48*, 60−103.
(89) Xiong, Y. J.; Xia, Y. N. Shape-controlled synthesis of metal nanostructures: The case of palladium. *Adv. Mater.* **2007**, *19*, 3385−3391.
(90) Whetten, R. L.; Shafigullin, M. N.; Khoury, J. T.; Schaaff, T. G.; Vezmar, I.; Alvarez, M. M.; Wilkinson, A. Crystal structures of molecular gold nanocrystal arrays. *Acc. Chem. Res.* **1999**, *32*, 397−406.
(91) Murray, C. B.; Kagan, C. R.; Bawendi, M. G. Self-organization of cdse nanocrystallites into 3-dimensional quantum-dot superlattices. *Science* **1995**, *270*, 1335−1338.
(92) Bentzon, M. D.; Vanwonterghem, J.; Morup, S.; Tholen, A.; Koch, C. J. W. Ordered aggregates of ultrafine iron-oxide particles - super crystals. *Philos. Mag. B* **1989**, *60*, 169−178.
(93) Cademartiri, L.; Ghadimi, A.; Ozin, G. A. Nanocrystal plasma polymerization: From colloidal nanocrystals to inorganic architectures. *Acc. Chem. Res.* **2008**, *41*, 1820−1830.
(94) Malakooti, R.; Cademartiri, L.; Akcakir, Y.; Petrov, S.; Migliori, A.; Ozin, G. A. Shape-controlled bi2s3 nanocrystals and their plasma polymerization into flexible film. *Adv. Mater.* **2006**, *18*, 2189−2194.
(95) Cademartiri, L.; von Freymann, G.; Arsenault, A. C.; Bertolotti, J.; Wiersma, D. S.; Kitaev, V.; Ozin, G. A. Nanocrystals as precursors for flexible functional films. *Small* **2005**, *1*, 1184−1187.
(96) Shaw, S.; Colaux, J. L.; Hay, J. L.; Peiris, F. C.; Cademartiri, L. Building materials from colloidal nanocrystal arrays: Evolution of structure, composition, and mechanical properties upon removal of ligands by o2 plasma. *Adv. Mater.* **2016**, *28*, 8900−8905.
(97) Shaw, S.; Yuan, B.; Tian, X.; Miller, K. J.; Cote, B. M.; Colaux, J. L.; Migliori, A.; Panthani, M. G.; Cademartiri, L. Building materials

DOI: 10.1021/acs.chemmater.7b02769
Chem. Mater. 2017, 29, 7888−7900

from colloidal nanocrystal arrays: Preventing crack formation during ligand removal by controlling structure and solvation. *Adv. Mater.* **2016**, *28*, 8892−8899.
(98) Talapin, D. V.; Yu, H.; Shevchenko, E. V.; Lobo, A.; Murray, C. B. Synthesis of colloidal pbse/pbs core-shell nanowires and pbs/au nanowire-nanocrystal heterostructures. *J. Phys. Chem. C* **2007**, *111*, 14049−14054.
(99) Carbone, L.; Nobile, C.; De Giorgi, M.; Sala, F. D.; Morello, G.; Pompa, P.; Hytch, M.; Snoeck, E.; Fiore, A.; Franchini, I. R.; Nadasan, M.; Silvestre, A. F.; Chiodo, L.; Kudera, S.; Cingolani, R.; Krahne, R.; Manna, L. Synthesis and micrometer-scale assembly of colloidal cdse/cds nanorods prepared by a seeded growth approach. *Nano Lett.* **2007**, *7*, 2942−2950.
(100) Li, J. J.; Wang, Y. A.; Guo, W.; Keay, J. C.; Mishima, T. D.; Johnson, M. B.; Peng, X. Large-scale synthesis of nearly monodisperse cdse/cds core/shell nanocrystals using air-stable reagents via successive ion layer adsorption and reaction. *J. Am. Chem. Soc.* **2003**, *125*, 12567−12575.
(101) Rakovich, Y. P.; Donegan, J. F.; Filonovich, S. A.; Gomes, M. J. M.; Talapin, D. V.; Rogach, A. L.; Eychmuller, A. Up-conversion luminescence via a below-gap state in cdse/zns quantum dots. *Phys. E (Amsterdam, Neth.)* **2003**, *17*, 99−100.
(102) Lu, Y.; Yin, Y.; Li, Z.-Y.; Xia, Y. Synthesis and self-assembly of au@sio2 core-shell colloids. *Nano Lett.* **2002**, *2*, 785−788.
(103) Dabbousi, B. O.; Rodriguez-Viejo, J.; Mikulec, F. V.; Heine, J. R.; Mattoussi, H.; Ober, R.; Jensen, K. F.; Bawendi, M. G. cdse)zns core-shell quantum dots: Synthesis and optical and structural characterization of a size series of highly luminescent materials. *J. Phys. Chem. B* **1997**, *101*, 9463−9475.
(104) Chen, Y.; Vela, J.; Htoon, H.; Casson, J. L.; Werder, D. J.; Bussian, D. A.; Klimov, V. I.; Hollingsworth, J. A. Giant" multishell cdse nanocrystal quantum dots with suppressed blinking. *J. Am. Chem. Soc.* **2008**, *130*, 5026−5027.
(105) Kovalenko, M. V.; Scheele, M.; Talapin, D. V. Colloidal nanocrystals with molecular metal chalcogenide surface ligands. *Science* **2009**, *324*, 1417−1420.
(106) Dolzhnikov, D. S.; Zhang, H.; Jang, J.; Son, J. S.; Panthani, M. G.; Shibata, T.; Chattopadhyay, S.; Talapin, D. V. Composition-matched molecular "solders" for semiconductors. *Science* **2015**, *347*, 425−428.
(107) Evans, A. G.; Cannon, R. M. Overview no. 48. *Acta Metall.* **1986**, *34*, 761−800.
(108) Garvie, R. C. Stabilization of the tetragonal structure in zirconia microcrystals. *J. Phys. Chem.* **1978**, *82*, 218−224.
(109) XRD characterization does not univocally allow for the distinction of tetragonal and cubic phase in nanocrystalline ZrO_2 due to the similarity of the two structures and peak broadening. Nonetheless, the tetragonal phase is more thermodynamically stable than the cubic phase at room temperature.
(110) Shaw, S.; Yuan, B.; Tian, X. C.; Miller, K. J.; Cote, B. M.; Colaux, J. L.; Migliori, A.; Panthani, M. G.; Cademartiri, L. Building materials from colloidal nanocrystal arrays: Preventing crack formation during ligand removal by controlling structure and solvation. *Adv. Mater.* **2016**, *28*, 8892−8899.
(111) Barr, T. L.; Seal, S. Nature of the use of adventitious carbon as a binding-energy standard. *J. Vac. Sci. Technol., A* **1995**, *13*, 1239−1246.
(112) Chastain, J.; King, R. C.; Moulder, J. *Handbook of X-ray photoelectron spectroscopy: A reference book of standard spectra for identification and interpretation of XPS data*; Physical Electronics Division, PerkinElmer Corp.: Eden Prairie, MN, 1995.
(113) Parmigiani, F.; Depero, L. E.; Sangaletti, L.; Samoggia, G. An xps study of yttria-stabilised zirconia single crystals. *J. Electron Spectrosc. Relat. Phenom.* **1993**, *63*, 1−10.
(114) Dengo, N.; Vittadini, A.; Natile, M. M.; Gross, S. Understanding surface chemistry of zinc sulfide colloids: A combined experimental and theoretical approach. In *The 2016 E-MRS Spring Meeting and Exhibit*, Lille, France, May 2−6, 2016; European Materials Research Society, 2016.
(115) Langford, J. I.; Wilson, A. J. C. Scherrer after sixty years: A survey and some new results in the determination of crystallite size. *J. Appl. Crystallogr.* **1978**, *11*, 102−113.
(116) Cademartiri, L.; Montanari, E.; Calestani, G.; Migliori, A.; Guagliardi, A.; Ozin, G. A. Size-dependent extinction coefficients of pbs quantum dots. *J. Am. Chem. Soc.* **2006**, *128*, 10337−10346.
(117) Huang, F.; Zhang, H. Z.; Banfield, J. F. Two-stage crystal-growth kinetics observed during hydrothermal coarsening of nanocrystalline zns. *Nano Lett.* **2003**, *3*, 373−378.
(118) Talapin, D. V.; Rogach, A. L.; Haase, M.; Weller, H. Evolution of an ensemble of nanoparticles in a colloidal solution: Theoretical study. *J. Phys. Chem. B* **2001**, *105*, 12278−12285.
(119) Voorhees, P. W. The theory of ostwald ripening. *J. Stat. Phys.* **1985**, *38*, 231−252.
(120) Volmer, M.; Weber, A. Germ-formation in oversaturated figures. *Z. Phys. Chem.* **1926**, *119U*, 277−301.
(121) Ostwald, W. Z. *Phys. Chem.* **1901**, *37*, 385.
(122) Ostwald, W. *Lehrbuch der allgemeinen chemie*; Verlag von Wilhelm Engelmann: Leipzig, Germany, 1896; Vol. *2*.
(123) Veshchunov, M. S. Modelling of grain growth kinetics in porous ceramic materials under normal and irradiation conditions. *Materials* **2009**, *2*, 1252−1287.
(124) Quach, D. V.; Avila-Paredes, H.; Kim, S.; Martin, M.; Munir, Z. A. Pressure effects and grain growth kinetics in the consolidation of nanostructured fully stabilized zirconia by pulsed electric current sintering. *Acta Mater.* **2010**, *58*, 5022−5030.
(125) Baldan, A. Review progress in ostwald ripening theories and their applications to nickel-base superalloys part i: Ostwald ripening theories. *J. Mater. Sci.* **2002**, *37*, 2171−2202.
(126) Chokshi, A. H. Diffusion, diffusion creep and grain growth characteristics of nanocrystalline and fine-grained monoclinic, tetragonal and cubic zirconia. *Scr. Mater.* **2003**, *48*, 791−796.
(127) Tekeli, S.; Erdogan, M.; Aktas, B. Influence of α-al2o3 addition on sintering and grain growth behaviour of 8 mol% y2o3-stabilised cubic zirconia (c-zro2). *Ceram. Int.* **2004**, *30*, 2203−2209.
(128) Goto, Y.; Omata, T.; Otsuka-Yao-Matsuo, S. Extremely suppressed grain growth of y2o3-stabilized zirconia nanocrystals synthesized by the nonhydrolytic sol−gel technique. *J. Electrochem. Soc.* **2009**, *156*, K4−K9.
(129) Mohapatra, P.; Shaw, S.; Mendivelso-Perez, D.; Bobbitt, J. M.; Silva, T. F.; Naab, F.; Yuan, B.; Tian, X. C.; Smith, E. A.; Cademartiri, L. Does Calcination Remove All Carbon From Colloidal Nanocrystal Assemblies? **2017**, submitted.
(130) Hay, J.; Crawford, B. Measuring substrate-independent modulus of thin films. *J. Mater. Res.* **2011**, *26*, 727−738.
(131) Kendall, K.; Alford, N. McN.; Birchall, J. D. A new method for measuring the surface-energy of solids. *Nature* **1987**, *325*, 794−796.

DOI: 10.1021/acs.chemmater.7b02769
Chem. Mater. 2017, 29, 7888−7900